HHS Public Access

Author manuscript

Nanomedicine (Lond). Author manuscript; available in PMC 2015 December 18.

Published in final edited form as:

Nanomedicine (Lond). 2014 December ; 9(18): 2803–2815. doi:10.2217/nnm.14.40.

Assessing the impact of engineered nanoparticles on wound healing using a novel *in vitro* bioassay

Enhua H Zhou[1,2,*], **Christa Watson**[1], **Richard Pizzo**[3,4], **Joel Cohen**[1], **Quynh Dang**[1], **Pedro Macul Ferreira de Barros**[5], **Chan Young Park**[1], **Cheng Chen**[6], **Joseph D Brain**[1], **James P Butler**[1,7], **Jeffrey W Ruberti**[8], **Jeffrey J Fredberg**[1], and **Philip Demokritout**[1,*]

[1]Department of Environmental Health, Harvard School of Public Health, Boston, MA 02115, USA

[2]Ophthalmology, Novartis Institutes of BioMedical Research, MA, USA (current affiliation)

[3]Department of Physics, Boston College, MA, USA

[4]New York Institute of Technology College of Osteopathic Medicine, NY, USA (current affiliation)

[5]Faculdade de Medicina, University of Sao Paulo, Brazil

[6]Center for Joint Surgery, Southwest Hospital, the Third Military Medical University, Chongqing, China

[7]Division of Sleep Medicine, Department of Medicine, Harvard Medical School and, Brigham & Women's Hospital, MA, USA

[8]Mechanical & Industrial Engineering, Northeastern University, MA, USA

Abstract

Aim—As engineered nanoparticles (ENPs) increasingly enter consumer products, humans become increasingly exposed. The first line of defense against ENPs is the epithelium, the integrity of which can be compromised by wounds induced by trauma, infection, or surgery, but the implications of ENPs on wound healing are poorly understood.

Materials & methods—Herein, we developed an *in vitro* assay to assess the impact of ENPs on the wound healing of cells from human cornea.

Results & discussion—We show that industrially relevant ENPs impeded wound healing and cellular migration in a manner dependent on the composition, dose and size of the ENPs as well as cell type. CuO and ZnO ENPs impeded both viability and wound healing for both fibroblasts and

*Authors for correspondence Tel.: +1 617 432 3481, ezhou@hsph.harvard.edu, pdemokri@hsph.harvard.edu.

Financial & competing interests disclosure

The authors have no other relevant affiliations or financial involvement with any organization or entity with a financial interest in or financial conflict with the subject matter or materials discussed in the manuscript apart from those disclosed.

No writing assistance was utilized in the production of this manuscript.

Authors' contributions

EH Zhou developed circular wound array bioassay and cell migration assays, performed experiments and analyzed data; EH Zhou and P Demokritou conceived the experiments and supervised their execution; EH Zhou, JJ Fredberg and P Demokritou drafted the manuscript; C Watson performed cell viability assay; J Cohen characterized particle powers and suspensions; R Pizzo, PMF de Barros, CY Park and C Chen assisted in sample preparation and imaging; JD Brain and JP Butler revised the manuscript; JW Rubert provided human corneal fibroblasts; all authors read and approved the final manuscript.

epithelial cells. Carboxylated polystyrene ENPs retarded wound healing of corneal fibroblasts without affecting viability.

Conclusion—Our results highlight the impact of ENPs on cellular wound healing and provide useful tools for studying the physiological impact of ENPs.

Keywords

corneal wound healing; engineered nanoparticles; high-throughput screening; nano-EHS; nanotechnology; nanotoxicology

The global nanotechnology (NT) industry reached over $US1.5 trillion last year, becoming a major economic force of the 21st century. A central ingredient of the NT industry are engineered nanoparticles (ENPs) [1,2]. The number of consumer products containing ENPs is growing at a similarly rapid pace, and is expected to reach 10,000 by the year 2020 [3]. ENPs can be found in paint coatings with a variety of submicron/nanoscale pigment (metal and oxide) powders [4]; toner formulations [5]; polymer- and carbon-matrix nanocomposites with montmorillonite clays, carbon nanotubes and graphene [6]; and sunscreens/cosmoceuticals. Thus, human exposure to ENPs becomes inevitable and has indeed been demonstrated [7,8]. Compared with micron-sized particulate matter, ENPs have greater potential to cross biological barriers to reach pulmonary connective tissues, lymphatics, blood circulation and critical organs [5,8–11]; they may also enter cells and be more biologically active due to their small size and large surface area [12–16]. Accordingly, potential deleterious effects of ENPs on human health have been reported, mostly focusing on the lung [9–10,17].

Much less attention has been given to the eye, which is directly exposed to the environment [18]. The cornea possesses an extraordinarily smooth surface, maintains the tear layer, transmits light, and protects the eye from pathogens and particulates. Exposure to air pollutants has been associated with increased conjunctival goblet cell hyper-plasia and ocular irritations [19,20]. Although the level of ocular exposure to ENPs remains to be quantified, ENPs are widely present in cosmetic products, such as sunscreens, makeups and contact lenses, which may result in ocular ENP exposure [8,21]. However, the impact of ENPs on the eye and resident cells remains poorly understood. Such impact may be minimal on an intact tissue and cells but exert a toll on a wounded tissue; indeed, humans with pre-existing airway or heart diseases are more susceptible to elevated air pollution [22]. However, a research area of nanotoxicology, which is lagging behind is the effect of ENPs on wounded cells with most of *in vitro* studies focusing primarily on healthy cells.

Herein, we present the development of a novel cellular bioassay to assess the impact of ENPs on wound healing for diverse types of ENPs and cells. The types of ENPs we used included copper oxide (CuO), zinc oxide (ZnO), silica dioxide (SiO_2) and titanium dioxide (TiO_2) ENPs, which are industry relevant and commonly used in a variety of products; fluorescent polystyrene (PS) particles were also used to investigate the role of particle size and uptake. The types of cells included human corneal limbal epithelial (HCLE) cells and human corneal fibroblasts (HCFs), which are important for corneal wound healing, and Madin–Darby canine kidney (MDCK) cells, which constitute a widely used model system

for investigating wound healing *in vitro*. Our results establish *in vitro* wound healing behavior as a physiological end point to evaluate the safety of ENPs.

Materials & methods

Wound array production

Polydimethylsiloxane (PDMS) membrane blocking has previously been used to create wounds in a cell monolayer with linear boundaries [23]. We extended this concept to create circular wounds in a 96-well format. To produce PDMS pillars, we first polymerized PDMS into a 6-mm-thick sheet (20:1 mixing ratio; Sylgard® 184; Dow Corning, MI, USA). We then punched this sheet with a 2-mm-diameter, circular, hollow indenter to produce pillars. Each pillar was attached to the center of a single well of a 96-well plate (Figure 1A; top).

Circular wound healing bioassay

We plated a variety of cells in these wound arrays and allowed them to grow into full confluence; due to the biocompatibility of PDMS cells in fact crawled onto the side of the pillar. The pillar was then pulled off, producing a 'wound' in the center of the monolayer (Figure 1A; middle). Each wound was imaged using an automated microscope (Leica DMI6000; Leica, Solms, Germany); it took approximately 10 min to image an entire 96-well plate. We developed a Matlab- based program to process the wound images and automatically detect wound edges. One example of a healing MDCK monolayer over 44 h is shown in Figure 1A (bottom). In order to automatically detect cell-covered regions, we combined image texture analysis and intensity thresholding. For MDCK cells, phase contrast images were used; for HCLE cells, 5-chloromethylfluorescein diacetate staining was used; for HCF cells, a combination of phase contrast, 5-chloromethylfluorescein diacetate staining, and F-actin staining (with Alexa Fluor® 488 Phalloidin, at 1/200 dilution; Invitrogen, CA, USA) were used. We call this 96-well plate wound-healing assay circular wound array bioassay (CWAB).

Single cell migration assay

We evaluated single cell migration by tracking fluorescently stained nuclei [24]. Cells were sparsely seeded at 30 cells/mm^2 in 96-well plates, allowed to incubate for 2 days, and then stained with 0.33–1 μg/ml Hoechst 33342 (Invitrogen) for 30 min. The stained cells were then treated with culture media containing 10% fetal bovine serum (FBS) as well as different doses of nanoparticles. A total of 18–24 h later, we imaged Hoechst-stained cell nuclei every 6 mins using an automated microscope (Leica DMI6000). Fluorescent exposure was minimized to avoid cell damage. We developed a Matlab-based program to track nuclei positions and to obtain the mean squared displacement for each cell.

Cell cultures & treatment

A variety of cells were used in this study in order to illustrate the versatility of the CWAB platform. We obtained immortalized human corneal-limbal epithelial (HCLE) cell line from IK Gipson, Schepens Eye Research Institute (MA, USA). These cells have been previously shown to possess the ability to differentiate and stratify *in vitro* [25]. We seeded these cells at 256 cells/mm^2 in supplemented keratinocyte serum-free medium (K-SFM; Invitrogen

17005–042) for 2–3 days for proliferation, and the media was then switched to DMEM/Nutrient Mixture F-12 (DMEM/F12) supplemented with 10% FBS and 10 ng/ml human recombinant EGF for 2–3 days for differentiation/stratification prior to wounding. The supplements to 500 ml K-FSM media included 1.25 ml bovine pituitary extract, 0.2 ng/ml EGF and 0.31 mM $CaCl_2$. MDCK cells (seeded at 500 cells/mm^2) and HCF cells (seeded at 256 cells/mm^2 unless stated otherwise) were cultured in low-glucose DMEM with 10% FBS for 3–4 days prior to wounding. HCF cells were isolated from human corneas [26] and used from passage 3 to passage 6. Cells were grown to confluence in 96-well plates with wound arrays as described above, the pillars were removed, the cells were washed once with PBS, and culture media containing 10% FBS as well as different doses of ENPs were added.

Panel of ENPs studied

We selected six ENPs for study, including both commercially available metal oxide ENPs currently used in consumer products such as paints, sunscreens and electronics, as well as PS beads of variable surface chemistry and primary particle size. In more detail: TiO_2 (25 nm; Aeroxide® from Evonik Degussa Corporation, NJ, USA), SiO_2 (55 nm; Evonik Degussa Corporation), CuO (less than 50 nm; Sigma-Aldrich, MO, USA), ZnO (40–100 nm; Alfa Aesar, MA, USA), carboxylate-modified PS FluoSpheres® (FS) of six sizes (20, 40, 100, 200, 500 and 1000 nm; emission/excitation of 580/605; Invitrogen), and carboxylated PS microspheres (60 nm; nonfluorescent; PC02N/6645 from Bangs Laboratories, IN, USA).

Characterization of ENPs

State-of-the-art analytical methods were used to characterize the properties of the ENPs. Nitrogen adsorption/Bruanuer–Emmet–Teller (BET) method (TriStar™; Micromeritics, GA, USA) was used to characterize specific surface area (SSA). The equivalent primary particle diameter, d_{BET}, was calculated as:

$$d_{BET}=6/(SSA \times \rho_p)$$

Where the particles were assumed to be spherical and ρ_p is the material density at 20°C. Particle diameter was also determined by x-ray diffraction (d_{XRD}). Supplementary Table 1 (see online at www.futuremedicine.com/doi/suppl/10.2217/NNM.14.40) summarizes the properties of the ENPs used in the study.

Preparation & characterization of ENP suspensions

For each ENP, we prepared stock suspensions at 10 mg/ml in double-distilled water. A total of 0.5–1 ml of each suspension was then sonicated for enough time in a sonicator (Vibra-Cell™ VCX 130; Sonics and Materials Inc., CT, USA) to break the agglomerates down to the primary particle level as described previously by the authors [16]. We then diluted these suspensions into cell culture media containing 10% FBS, which helped to stabilize the suspension and minimized nanoparticle reagglomeration during the experiment [16,27]. Suspended ENPs were applied to cells within 1 h of preparation unless otherwise stated. For all species of ENPs suspended in cell culture media, we used dynamic light scattering (Malvern Zetasizer Nano-ZS; Malvern Instruments, Worcestershire, UK) to measure for

hydrodynamic diameter, polydispersity index and zeta-potential (see Table 1). We used ENP doses varying from 0 to 108 μg/ml. When necessary, we performed linear interpolation to map results in between doses.

Cell viability & proliferation

3-[4,5-dimethylthiazol-2-yl]-2,5-diphenyl tetrazolium bromide (MTT) assay (Roche, Basel, Switzerland) and Alamar Blue assay (Invitrogen) were used to assess cell viability for each ENP, dose and cell line. Cells were cultured, wounded and treated with ENPs for 18 h. For MTT assay, cell media was replaced with 100 μl/well of fresh media, and then treated with MTT reagent (10 μl/well) for 4 h at 37°C. Solubilization reagent (100 μl) was added to dissolve the formazan crystals produced from the reduction of the tetrazolium salt or MTT reagent. The absorbance of each sample was measured using a microplate reader (Biotek Instruments, VT, USA) at 550 nm. To account for possible reagent–particle interaction, concurrent no-cell assays were performed in triplicate and resulting optical densities were subtracted as background. We then calculated viability relative to untreated cells, which served as 100% viability control. For Alamar Blue assay, we first imaged the plate at excitation/emission of 544/590 nm (Fluoroskan Ascent™ Plate Reader; ThermoFisher, MA, USA) to obtain the background value. Alamar Blue was then added to each well at 10% volume and incubated for 90 min before the plate was imaged again. We then subtracted the final signal by the background signal and then calculated viability relative to 100% viable controls (untreated cells) and 0% viable control (0.1% saponin-treated cells). To measure cell proliferation, we used CyQUANT® assay (Invitrogen). HCF cells were plated at 30 cells/mm^2 on day 1, treated with ENPs on day 2, and CyQUANT assay was performed on day 3 according to manufacturers instructions.

Uptake of carboxylate-modified PS FS

Confluent cells were treated for 1 day with 12 μg/ml of carboxylated FS of two sizes, and then subjected to either fixation alone or simultaneous fixation and permeabilization before particle fluorescence was quantified using a plate reader at the appropriate wavelength (Fluoroskan Ascent Plate Reader).

Statistical analysis

Data were compared by one-way analysis of variance or by Student's *t*-test with two tails and unequal variance. A difference was considered significant if $p < 0.05$. Such statistical significance is achieved between two groups when their 95% CIs do not overlap [28]. Hence, we plotted data with 95% CIs, which correspond to mean ±1.96 standard error of the mean. If the error bars of two data points do not overlap, they are statistically different [28].

Results

Circular wound array bioassay

The CWAB bioassay was used to address the impact of ENPs on wound healing and the collective migratory behavior of a variety of cell lines. As described in detail in the method section, the CWAB assay is based on the PDMS stamp technique that produces wounds with controlled geometry [23,29]. Figure 1A illustrates how CWAB was applied in the case of a

96-well format, using PDMS pillars (6 mm in height and 2 mm in diameter) and applied them to block a circular area in each well of a 96-well plate (Figure 1A and see 'Materials & methods' section). By growing cells to confluence and peeling off the pillars, we were able to create 96 wounds with uniform geometry and simultaneously track the healing of these wounds over time using automated microscopy (Figure 1B and see 'Materials & methods' section). The microscopic images were analyzed using a Matlab-based code developed in house to quantify the wound areas (Figure 1A). It is worth noting that the CWAB bioassay is, in principle, similar to Oris™ Cell Migration Assay [30], but more flexible and far less costly.

Wound healing behavior of three different cell types

In order to demonstrate the versatility of the proposed *in vitro* approach, the CWAB system was used to assess wound healing of three cell types: HCLE cells, HCFs and MDCK type II epithelial cells; the MDCK cells were included here as a widely studied model cell type [29]. We demonstrated that in the absence of ENP exposures, wound area decreased with time in a largely linear fashion (Figure 1C), consistent with previous reports on MDCK cells [29]. HCLE cells closed 2-mm wounds within 1 day and MDCK cells within 2 days; by contrast, primary HCF cells took 3 days (HCF48 from a 48-year-old donor) or much longer (HCF52 from a 52-year-old donor) to close the wound (Figure 1C). This drastic difference in wound healing rate (analysis of variance; $p < 0.0001$) between different cell types likely reflects the phenotypic differences between epithelial cells and fibroblasts.

ENP characterization

The panel of ENPs investigated in this study was characterized both in the dry powder form as well as in their liquid suspension state using state of the art analytical methods, as described in detail in the Methods section. Supplementary Table 1 summarizes the properties of the used ENPs.

Consistent with previous reports, most ENPs that have primary particle sizes below 100 nm appeared to form complexes of 140–460 nm in the serum-containing media, with the exception of ZnO ENPs suspended in DMEM with 10% FBS, which formed agglomerates above 1 μm, and TiO_2, which formed agglomerates above 800 μm in both media. Such large and polydisperse agglomeration of ENPs is known to occur in certain nanoparticle/media systems, including ZnO ENPs in DMEM media [16,31–33]. Additionally, large differences in agglomerate size were observed between the amine- modified PS spheres and carboxyl-modified PS spheres (Table 1), likely due to differences in their surface charges and the subsequent effects on electrostatic stabilization of suspended agglomerates [16,34]. Particle size distribution did not change significantly over 24 h of suspension (Supplementary Figure 1). These freshly prepared and well-characterized ENP suspensions were then applied to cells immediately after the wounding. It is worth noting that two of the ENPs used here, namely ZnO and CuO, can partially be dissolved in culture media and release ions [35,36].

ENPs can inhibit wound healing via decreasing cell viability

We first examined the effects of CuO ENPs on each cell type. For all ENPs, we tested doses ranging from 4 to 108 μg/ml. In a dose-dependent manner, CuO ENPs reduced cell viability

with median lethal doses (LD50) of 6.3–20.3 μg/ml (Figure 2C,i), which is in line with previous reports [37,38]. Using the CWAB assay, we found that these particles dose-dependently inhibited wound healing in monolayers of HCLE and MDCK cells with median effective doses (ED50) of 16.1 and 51.3 μg/ml, respectively (Figure 2). Furthermore, they entirely inhibited the migration of HCF cells at the lowest dose tested of 4 μg/ml (Figure 2), in fact causing the wound area to expand (Figure 2A) and relative wound healing to become negative. The relative healing was defined as the fractional reduction in wound area normalized by that achieved by untreated cells:

$$-\text{that is}, (A_0 - A_{treated})/(A_0 - A_{untreated})$$

Where $A_{treated}$ and $A_{untreated}$ are the final wound area for treated and untreated cells, respectively. These data are consistent with the notion that ENPs may inhibit wound healing through cytotoxicity.

To further confirm the inhibitory effect of cytotoxic ENPs on wound healing, we turned to ZnO nanoparticles; ZnO particles have high toxicity on HCLE cells (LD50 of 23.1 μg/ml), but much less toxicity on HCF cells (LD50 >100 μg/ml) (Figure 2C,ii). ZnO particles potently inhibited wound closure in HCLE monolayers with ED50 of 15.8 μg/ml (Figure 2B,ii). Their impact on the other cell types was much less: the ED50 was 45.2 μg/ml for HCF48 cells and beyond 100 μg/ml for HCF52 and MDCK cells (Figure 2B,ii). Again, wound expansion was observed at high ENP doses for HCLE and HCF48 cells, evidenced by the negative values of relative healing (Figure 2B,ii). We note that ZnO ENPs formed large agglomerates in the DMEM media, which were used for HCF and MDCK cells, but considerably better in the DMEM/F12 media, which were used for HCLE cells (Table 1). It remains to be explored whether the better dispersion in the latter media led to a higher toxicity for the latter cell type. Nonetheless, our previous finding that the primary size of ZnO particles does not affect their biological impact or toxicity on human airway smooth muscle cells would argue against that [38].

We then explored the extent to which reduced healing is associated with reduced cell viability. For both ZnO and CuO ENPs, reduced viability is generally associated with reduced healing (Figure 2C,ii). However, reduction in the latter can greatly exceed that in the former (Figure 2C,ii). This is because relative viability cannot go below zero, but relative healing can do so as a wound expands or cells shrink. As such, relative healing could provide a more sensitive measure of the physiological impact of ENPs, which could cause morphological changes without impacting viability.

ENPs can also inhibit wound healing without affecting cell viability

Even in the absence of cytotoxicity, nanoparticles may physically interact with cells and slow down their movement in a nonspecific manner, which leads to the question of whether wound healing can be impeded without a reduction in cell viability. We initially studied amorphous SiO_2 nanoparticles; these particles had little impact on cell viability (Supplementary Figure 2). Interestingly, even at 108 μg/ml, they did not decrease wound

healing by more than 20%. These data suggest that not every species of ENP interferes with cell migration and wound healing.

The next nontoxic ENP that we looked at was 40 nm PS nanoparticles that are fluorescent (excitation/emission = 580/605 nm) and carboxylate-modified (FS^{40nm}). FS^{40nm} particles did not decrease cell viability up to 108 μg/ml (Figure 3C). They did not appreciably slow down the wound healing of HCLE or MDCK cells. However, they slowed down the wound healing of HCF cells from both donors by up to 55% and in a dose-dependent manner (Figure 3; ED50 is approximately 85 μg/ml for both cells). These results were surprising, and led to the question of whether they could be attributed to the fluorescent nature of the particles. When 60-nm PS nanoparticles that also are carboxylated but not fluorescent (PS^{60nm}) were applied to the same cells, the results were qualitatively the same: little impact on MDCK or HCLE cells, but a dose-dependent inhibition on HCF wound healing (ED50: 60.7 μg/ml for HCF52; Supplementary Figure 3). This phenotypic impact of the carboxylated PS particles echoes a previous study that demonstrated their effect on iron absorption after oral exposure [39]. Together, our data demonstrate that ENPs can impede wound healing in a cell- and particle-type dependent manner, even in the absence of cytotoxicity.

Different cell types exhibited distinct patterns of particle uptake

The difference in wound healing responses to various ENPs among the three cell types was striking, leading to the question of whether this difference could be attributable to particle uptake. Particle uptake was assessed using fluorescence microscopy after the application of FS^{40nm} particles. Since we fixed and permeabilized the cells simultaneously, particles that were bound to the plasma membrane were mostly removed. We therefore considered the majority of the remaining particles to be either internalized or cytoskeleton-bound. These particles were uniformly taken up by HCF cells (Figure 3D); by contrast, MDCK and HCLE cells only took up those particles at the leading edge of the healing wound (Figure 3D & Supplementary Figure 4A). It is worth noting that such endocytic/phagocytic activity by the leading cells had little impact on the overall wound healing rate of MDCK and HCLE cells.

In the absence of a wound, HCF cells exhibited approximately ten-times more uptake of those carboxylated FS particles than HCLE cells ($p < 0.001$, Figure 3E); same results were obtained whether we permeabilize the cells or not (compare Figure 3E with Supplementary Figure 4B). This elevated particle uptake potentially contributes to the larger decrease in the wound healing rate of the HCF cells. Future work on the cell type-specific mechanism of ENP uptake is warranted.

Effect of FS particles on single cell migration of HCF cells

To understand the mechanism by which ENPs impede wound closure in HCF cells, we first looked at cell proliferation. To our surprise, even at the maximum particle doses used, cell proliferation was not affected (Supplementary Figure 5). We then hypothesized that the impairment is due to impediment of individual cell migration. Cell migration was assessed by tracking the motion of fluorescently labeled cell nuclei (Figures 4A,ii & 4A,iii). The

mean squared displacement (MSD) of the nuclei increased with time intervals following a power law function:

$$MSD = D\frac{\Delta t^{\alpha}}{10}$$

(Figure 4A,iv)

Here, *D* is the characteristic MSD at Δt = 10 mins, and therefore represents instantaneous cell speed ($D \sim [v\Delta t)^2]$); α equals 1 for Brownian motion and 2 for straightforward (ballistic) motion, and therefore represents the directional persistence of migration. Decreases in either or both of these two parameters can lead to reduced wound healing [40].

Without any treatment, HCF48 cells had a slightly lower α, but a much higher *D* than HCF52 cells ($p < 0.001$; gray markers in Figure 4); this suggests HCF48 may execute faster wound healing, which is indeed what we have observed ($p < 0.001$; Figure 1C). When these cells were treated with FS^{40nm} (108 μg/ml; green circles in Figure 4), their MSD, α and *D* were all reduced ($p < 0.001$). These data are consistent with the notion that the rate of wound healing of HCF fibroblasts is largely determined by the rate of single cell migration, and indicate that the interference of single cell migration by FS particles perhaps account for their impediment of HCF wound healing.

Since single cell migration can be characterized by α and *D*, we next asked which of the two parameters is more severely impacted by FS particles. When treated with FS^{40nm}, α was reduced by less than 0.1 for both HCF48 ($\alpha = 1.48 \pm 0.01$ if untreated) and HCF52 ($\alpha = 1.56 \pm 0.03$ if untreated; Figure 4B); by contrast, *D* was reduced by approximately 50% for both cell strains ($p < 0.001$; Figure 4C), a reduction quantitatively similar to that observed in wound healing assay (Figure 3B, black triangles). These data suggest that compared with directional persistence, cell speed is more severely impacted by FS particles.

To further confirm that the particle-impaired wound healing rate is mainly due to reduced cell speed, we systematically varied particle size, which is known to be a major determinant of cell–nanoparticle interaction for a wide range of particle species [41]. When six FS particle species ranging from 20 to 1000 nm in diameter were applied to the cells at 108 μg/ml, we found that all particles at or below 500 nm decreased MSD at long time intervals ($p < 0.001$; Figure 4A). α generally decreased with decreasing particle size, reaching a maximal decrease of 0.15 and 0.16 for HCF52 and HCF48, respectively, at the smallest particle size of 20 nm (Figure 4B). On the other hand, *D* exhibited a step-like decrease as the particle size decreases from 1000 to 500 nm, reaching a plateau of approximately 50% baseline at smaller particle sizes ($p < 0.001$ compared with control; Figure 4C). When wound healing rate was measured using CWAB assay with the same cells treated with the same particles, the relative healed area at 87 h exhibited a size dependence that was more similar to that for *D* than to that for α (compare Figure 4D with Figures 4B & Figure 4C); this was interesting because there was no *a priori* prediction as to which parameter, *D* or α, controls the rate of wound healing. The carboxylated PS^{60nm} nanoparticles that are not

fluorescent behaved entirely similar to the FS particles (Figures 4B–4D, solid symbols), again suggesting that the particle effects are not due to particle fluorescence.

When we quantitatively correlated relative healed area with α and with *D* for HCF52, there was a statistically significant correlation between wound healing and α (correlation coefficient = 0.70; p = 0.005; circles in Figure 4E); however, the data points were scattered, giving rise to large uncertainty in the fitted line (slope = 2.47 ± 1.59; 95% CI). By contrast, there was a stronger correlation between wound healing and *D* (correlation coefficient = 0.86; p = 7e-5; circles in Supplementary Figure 6); the intercept of the fitted line was not statistically different from 0, suggesting direct proportionality between relative healed area and *D* (left dash line in Supplementary Figure 6). Similar observations were also made of HCF48 (triangles in Figure 4E & Supplementary Figure 6). When we normalized *D* by that of untreated cells, strikingly, the relative cell speed was overall identical to relative healing for two cell strains, for low and high particle doses, and for seven particle types (Figure 4F). Collectively, our data strongly suggest that carboxylated PS particles, while not impacting cell viability, can impede wound healing of HCF cells by reducing the migration speed at the single-cell level.

Discussion

Little is known about the impact of ENPs on wound healing in general. Here we presented an *in vitro* platform that can be used to assess the impact of ENPs on cell migration and wound healing. It was demonstrated that industrially relevant ENPs can impede wound healing by means of reduced cellular viability. Furthermore, interestingly, in the absence of toxicity carboxylated PS particles impeded wound healing as well as single cell migration in a manner dependent on particle size, dose and cell type. Importantly, fibroblasts were more severely slowed by those particles than were epithelial cells, a difference potentially attributable to the much higher particle uptake by the fibroblasts. Investigating the mechanism by which carboxylated PS ENPs impeded wound healing of corneal fibroblasts, we discovered that it is mainly attributable to a reduction in instantaneous cell speed instead of directional persistence.

Our results reveal that not every nanoparticle species influences the rate of wound healing. SiO_2 ENPs did not alter that rate at doses up to 100 μg/ml. By contrast, ZnO and CuO ENPs inhibited cell viability as well as wound healing rate. Since these materials are relatively soluble [42], it is likely that the soluble ions contribute considerably to the physiological impact of these particles and the effect of dissolution kinetics on wound healing should be further studied in future mechanistic studies. PS ENPs have negligible solubility [43], and yet we observed particle size dependent impact on wound healing rate. The mechanism awaits further investigation.

Furthermore, the mechanism by which ENPs reduce the instantaneous cell speed and directionality is of interest. Cell migration is an orchestrated process that involves cell–cell and cell–extracellular matrix adhesion, cytoskeletal remodeling, signaling networks and physical forces [44–46]. We have previously demonstrated that mechanical properties and contractile responses of human airway smooth muscle cells are affected by nanoparticles in

a dose- and size-dependent manner [38]. It is tempting to suggest that one mechanism by which nanoparticles impede wound healing is by changing cellular mechanical properties and force generation [38,47], both of which are known to modulate collective migration in epithelial and endothelial cells [45–46,48]. Alternatively, nanoparticles are known to generate reactive oxygen species (ROS) [49], which can lead to microtubule remodeling [50], thereby affecting cell migration. Nonetheless, examination of the morphology of microtubules (both acetylated and total alpha tubulin) and F-actin did not reveal any modification by the carboxylated PS particles (data not shown). The detailed mechanism by which nanoparticles slow down cell migration awaits further investigation.

Two major limitations of our *in vitro* wound healing model relate to the lack of inflammation and extracellular matrix dynamics that are key determinants of wound healing outcomes *in vivo*. For example, although nano-crystalline silver demonstrated cytotoxicity and inhibited migration, it in fact improved wound healing *in vivo* [51]. This improved wound healing trajectory is attributed to the antimicrobial properties, reduced levels of matrix metalloproteinases, balanced reactive oxygen species and, ultimately, reduced inflammation [51,52]. In addition, our *in vitro* cell culture model does not capture the complex architecture, composition and mechanical compliance of the extra-cellular matrix, all of which are known to regulate wound healing and tissue regeneration [53]. Extracellular matrix may be directly modified by ENPs and may modulate the response to ENPs by resident cells. These limitations of *in vitro* wound healing models clearly need to be addressed by using *in vivo* models and/or 3D tissue-engineered models. Despite these limitations, our *in vitro* model helps to define mechanisms at the cellular level and provides a preliminarily yet efficient means to assess the physiological impact of ENPs.

Conclusion & future perspective

The cell-based assays described here establish a novel platform to quantify the effects of ENPs on wound healing and single cell migration. These processes are necessary for the integrity and homeostasis of various epithelium-lined organs, which include the lung, the skin, the gut and the eye. Our work suggests wound healing can be a key process that is impacted by ENPs. Future work will determine the extent to which our *in vitro* assays of wound healing and cell migration mimic *in vivo* physiology in the context of ENP exposure, ultimately identifying ENP species that inhibit or promote wound healing.

Supplementary Material

Refer to Web version on PubMed Central for supplementary material.

Acknowledgements

The authors thank I Gipson for providing human corneal epitheial cells and R Zareian for preparing human corneal fibroblasts.

This research was supported by Harvard School of Public Health – National Institute of Environmental Health Sciences Center for Environmental Health (ES000002) and the National Science Foundation (award ID 1235806).

References

Papers of special note have been highlighted as:

• of interest

•• of considerable interest

1. BCC Research. Nanotechnology: a realistic market assessment. NAN031D. 2010. http://www.bccresearch.com/market-research/nanotechnology/nanotechnology-realistic-market-assessment-nan031d.html
2. BCC Research. Nanotechnology research review. NAN04713. 2011. www.bccresearch.com/market-research/nanotechnology/2011-nanotechnology-review-nan047c.html
3. Project on Emerging Nanotechnologies: The Nanotechnology Consumer Product Inventory. 2011. www.nanotechproject.org/cpi
4. Kokonou M, Rebholz C, Giannakopoujos KP, Doumanidis CC. Low aspect-ratio porous alumina templates. Microelec. Eng. 2008; 85(5–6):1186–1188.
5. Bello D, Martin J, Santeufemio C, et al. Physicochemical and morphological characterisation of nanoparticles from photocopiers: implications for environmental health. Nanotoxicology. 2012; 7(5):989–1003. [PubMed: 22551088]
6. Drakonakis VM, Velisaris CN, Seferis JC, Doumanidis CC, Wardle BL, Papanicolaou GC. Matrix hybridization in the interlayer for carbon fiber reinforced composites. Polymer Composites. 2010; 31(11):1965–1976.
7. Landsiedel R, Ma-Hock L, Kroll A, et al. Testing metal-oxide nanomaterials for human safety. Adv. Mater. 2010; 22(24):2601–2627. [PubMed: 20512811]
8. Kessler R. Engineered nanoparticles in consumer products: understanding a new ingredient. Environ. Health Perspect. 2011; 119(3):a120–a125. [PubMed: 21356630]
9. Nel A, Xia T, Madler L, Li N. Toxic potential of materials at the nanolevel. Science. 2006; 311(5761):622–627. [PubMed: 16456071]
10. Demokritou P, Gass S, Pyrgiotakis G, et al. An *in vivo* and *in vitro* toxicological characterisation of realistic nanoscale CeO_2 inhalation exposures. Nanotoxicology. 2013; 7(8):1338–1350. [PubMed: 23061914]
11. Pirela S, Molina R, Watson C, et al. Effects of copy center particles on the lungs: a toxicological characterization using a Balb/c mouse model. Inhal. Toxicol. 2013; 25(9):498–508. [PubMed: 23895351] •• Photocopiers and printers may represent an important source of daily engineered nanoparticle (ENP) exposure.
12. Hamilton RF Jr, Wu N, Porter D, Buford M, Wolfarth M, Holian A. Particle length-dependent titanium dioxide nanomaterials toxicity and bioactivity. Part. Fibre Toxicol. 2009; 6:35. [PubMed: 20043844]
13. Larsen ST, Roursgaard M, Jensen KA, Nielsen GD. Nano titanium dioxide particles promote allergic sensitization and lung inflammation in mice. Basic Clin. Pharmacol. Toxicol. 2010; 106(2):114–117. [PubMed: 19874288]
14. Li JJE, Muralikrishnan S, Ng C-T, Yung L-YL, Bay B-H. Nanoparticle-induced pulmonary toxicity. Exp. Biol. Med. 2010; 235(9):1025–1033.
15. Poland CA, Duffin R, Kinloch I, et al. Carbon nanotubes introduced into the abdominal cavity of mice show asbestos-like pathogenicity in a pilot study. Nat. Nanotechnol. 2008; 3(7):423–428. [PubMed: 18654567]
16. Cohen J, Deloid G, Pyrgiotakis G, Demokritou P. Interactions of engineered nanomaterials in physiological media and implications for *in vitro* dosimetry. Nanotoxicology. 2013; 7(4):417–431. [PubMed: 22393878]
17. Wiesner MR. Responsible development of nanotechnologies for water and wastewater treatment. Water Sci. Technol. 2006; 53(3):45–51. [PubMed: 16605016]
18. Torricelli AA, Novaes P, Matsuda M, Alves MR, Monteiro MLR. Ocular surface adverse effects of ambient levels of air pollution. Arq. Bras. Oftalmol. 2011; 74(5):377–381. [PubMed: 22184003]

19. Novaes P, Do Nascimento Saldiva PH, Kara-Jose N, et al. Ambient levels of air pollution induce goblet-cell hyperplasia in human conjunctival epithelium. Environ. Health Perspect. 2007; 115(12):1753–1756. [PubMed: 18087595] •• One of the first studies indicating the negative effects of ambient particulates on the eye surface.
20. Novaes P, Saldiva PH, Matsuda M, et al. The effects of chronic exposure to traffic derived air pollution on the ocular surface. Environ. Res. 2010; 110(4):372–374. [PubMed: 20338555]
21. Lorenz C, Von Goetz N, Scheringer M, Wormuth M, Hungerbuhler K. Potential exposure of German consumers to engineered nanoparticles in cosmetics and personal care products. Nanotoxicology. 2011; 5(1):12–29. [PubMed: 21417685] •• Quantitative information about human exposure to ENPs in different parts of the body.
22. Nel A. Atmosphere. Air pollution-related illness: effects of particles. Science. 2005; 308(5723): 804–806. [PubMed: 15879201]
23. Poujade M, Grasland-Mongrain E, Hertzog A, et al. Collective migration of an epithelial monolayer in response to a model wound. Proc. Natl Acad. Sci. USA. 2007; 104(41):15988–15993. [PubMed: 17905871] •• Innovative creation of wounds with defined geometry using rubber stamps.
24. Zahm JM, Kaplan H, Herard AL, et al. Cell migration and proliferation during the *in vitro* wound repair of the respiratory epithelium. Cell Motil. Cytoskeleton. 1997; 37(1):33–43. [PubMed: 9142437]
25. Gipson IK, Spurr-Michaud S, Argueso P, Tisdale A, Ng TF, Russo CL. Mucin gene expression in immortalized human corneal-limbal and conjunctival epithelial cell lines. Invest. Ophthalmol. Vis. Sci. 2003; 44(6):2496–2506. [PubMed: 12766048] • Generation of the human corneal limbal epithelial cell line.
26. Guo X, Hutcheon AE, Melotti SA, Zieske JD, Trinkaus-Randall V, Ruberti JW. Morphologic characterization of organized extracellular matrix deposition by ascorbic acid-stimulated human corneal fibroblasts. Invest. Ophthalmol. Vis. Sci. 2007; 48(9):4050–4060. [PubMed: 17724187]
27. Ji Z, Jin X, George S, et al. Dispersion and stability optimization of TiO_2 nanoparticles in cell culture media. Environ. Sci. Technol. 2010; 44(19):7309–7314. [PubMed: 20536146]
28. Payton ME, Greenstone MH, Schenker N. Overlapping confidence intervals or standard error intervals: what do they mean in terms of statistical significance? J. Insect. Sci. 2003; 3:34. [PubMed: 15841249]
29. Anon E, Serra-Picamal X, Hersen P, et al. Cell crawling mediates collective cell migration to close undamaged epithelial gaps. Proc. Natl Acad. Sci. USA. 2012; 109(27):10891–10896. [PubMed: 22711834]
30. Gough W, Hulkower KI, Lynch R, et al. A quantitative, facile, and high-throughput image-based cell migration method is a robust alternative to the scratch assay. J. Biomol. Screen. 2011; 16(2): 155–163. [PubMed: 21297103]
31. Deng X, Luan Q, Chen W, et al. Nanosized zinc oxide particles induce neural stem cell apoptosis. Nanotechnology. 2009; 20(11):115101. [PubMed: 19420431]
32. Reed RB, Ladner DA, Higgins CP, Westerhoff P, Ranville JF. Solubility of nanozinc oxide in environmentally and biologically important matrices. Environ. Toxicol. Chem. 2012; 31(1):93–99. [PubMed: 21994124]
33. Everett WN, Chern C, Sun D, et al. Phosphate-enhanced cytotoxicity of zinc oxide nanoparticles and agglomerates. Toxicol. Lett. 2014; 225(1):177–184. [PubMed: 24362007]
34. Derjaguin B. Theory of the stability of strongly charged lyophobic sols and the adhesion of strongly charged particles in solutions of electrolytes. Acta Physicochim. USSR. 1941; 14:633–662.
35. Studer AM, Limbach LK, Van Duc L, et al. Nanoparticle cytotoxicity depends on intracellular solubility: comparison of stabilized copper metal and degradable copper oxide nanoparticles. Toxicol. Lett. 2010; 197(3):169–174. [PubMed: 20621582]
36. Zhang H, Ji Z, Xia T, et al. Use of metal oxide nanoparticle band gap to develop a predictive paradigm for oxidative stress and acute pulmonary inflammation. ACS Nano. 2012; 6(5):4349–4368. [PubMed: 22502734] • A new theory of nanotoxicity is proposed with experimental support.

37. Fahmy B, Cormier SA. Copper oxide nanoparticles induce oxidative stress and cytotoxicity in airway epithelial cells. Toxicol. In Vitro. 2009; 23(7):1365–1371. [PubMed: 19699289]
38. Berntsen P, Park CY, Rothen-Rutishauser B, et al. Biomechanical effects of environmental and engineered particles on human airway smooth muscle cells. J. R. Soc. Interface. 2010; 7(Suppl. 3):S331–S340. [PubMed: 20356875] •• One of the first papers demonstrating an alteration of cell contractility caused by ENPs.
39. Mahler GJ, Esch MB, Tako E, et al. Oral exposure to polystyrene nanoparticles affects iron absorption. Nat. Nanotechnol. 2012; 7(4):264–271. [PubMed: 22327877]
40. Petrie RJ, Doyle AD, Yamada KM. Random versus directionally persistent cell migration. Nat. Rev. Mol. Cell Biol. 2009; 10(8):538–549. [PubMed: 19603038]
41. Oberdorster G, Oberdorster E, Oberdorster J. Nanotoxicology: an emerging discipline evolving from studies of ultrafine particles. Environ. Health Perspect. 2005; 113(7):823–839. [PubMed: 16002369]
42. Xia T, Kovochich M, Liong M, et al. Comparison of the mechanism of toxicity of zinc oxide and cerium oxide nanoparticles based on dissolution and oxidative stress properties. ACS Nano. 2008; 2(10):2121–2134. [PubMed: 19206459]
43. Xia T, Kovochich M, Liong M, Zink JI, Nel AE. Cationic polystyrene nanosphere toxicity depends on cell-specific endocytic and mitochondrial injury pathways. ACS Nano. 2008; 2(1):85–96. [PubMed: 19206551]
44. Cordeiro JV, Jacinto A. The role of transcription-independent damage signals in the initiation of epithelial wound healing. Nat. Rev. Mol. Cell Biol. 2013; 14(4):249–262.
45. Mihai C, Bao S, Lai JP, Ghadiali SN, Knoell DL. PTEN inhibition improves wound healing in lung epithelia through changes in cellular mechanics that enhance migration. Am. J. Physiol. Lung Cell. Mol. Physiol. 2012; 302(3):L287–L299. [PubMed: 22037358]
46. Kim JH, Serra-Picamal X, Tambe DT, et al. Propulsion and navigation within the advancing monolayer sheet. Nat. Mater. 2013; 12(9):856–863. [PubMed: 23793160]
47. Buyukhatipoglu K, Clyne AM. Superparamagnetic iron oxide nanoparticles change endothelial cell morphology and mechanics via reactive oxygen species formation. J. Biomed. Mater. Res. A. 2011; 96(1):186–195. [PubMed: 21105167]
48. Tambe DT, Hardin CC, Angelini TE, et al. Collective cell guidance by cooperative intercellular forces. Nat. Mater. 2011; 10(6):469–475. [PubMed: 21602808]
49. Muller L, Riediker M, Wick P, Mohr M, Gehr P, Rothen-Rutishauser B. Oxidative stress and inflammation response after nanoparticle exposure: differences between human lung cell monocultures and an advanced three-dimensional model of the human epithelial airways. J. R. Soc. Interface. 2009; 7(Suppl. 1):S27–S40. [PubMed: 19586954] • 3D cell coculture provides better recapitulation of the native tissue structure for nanotoxicology studies.
50. Apopa PL, Qian Y, Shao R, et al. Iron oxide nanoparticles induce human microvascular endothelial cell permeability through reactive oxygen species production and microtubule remodeling. Part. Fibre Toxicol. 2009; 6:1. [PubMed: 19134195]
51. Wright JB, Lam K, Buret AG, Olson ME, Burrell RE. Early healing events in a porcine model of contaminated wounds: effects of nanocrystalline silver on matrix metalloproteinases, cell apoptosis, and healing. Wound Repair Regen. 2002; 10(3):141–151. [PubMed: 12100375]
52. Atiyeh BS, Costagliola M, Hayek SN, Dibo SA. Effect of silver on burn wound infection control and healing: review of the literature. Burns. 2007; 33(2):139–148. [PubMed: 17137719]
53. Schultz GS, Wysocki A. Interactions between extracellular matrix and growth factors in wound healing. Wound Repair Regen. 2009; 17(2):153–162. [PubMed: 19320882]

Executive Summary

Background

- The human cornea represents a key exposure site for pollutants and engineered nanoparticles (ENPs), but we know little about their pathophysiological consequences.
- ENPs may impact the normal wound healing process, but such impacts have not been explored.

Materials & methods

- We developed circular wound array bioassay and single cell migration assay, both in 96-well plate format.

Results

- CuO ENPs impede wound healing of both epithelial cells and fibroblasts, with a greater impact on the fibroblasts.
- ZnO ENPs had smaller impact on human corneal fibroblasts than on the human corneal limbal epithelial cells.
- SiO_2 ENPs did not affect the viability or wound healing of any cell type at up to 108 ug/ml.
- Carboxylated polystyrene ENPs did not affect cell viability, had no impact on the wound healing of epithelial cells, but retarded wound healing and single cell migration of human corneal fibroblasts.
- Human corneal fibroblasts exhibited much greater uptake of carboxylated polystyrene ENPs than did human corneal limbal epithelial cells.
- Smaller carboxylated polystyrene ENPs had a greater impact on the wound healing and single cell migration of human corneal fibroblasts.

Conclusion

- The circular wound array bioassay and single cell migration assays developed here can serve as physiologically relevant tools for evaluating biological activities of nanoparticles on wounded cells.

Future perspective

- The circular wound array bioassay provides an efficient method to evaluate the pathophysiological impact of thousands of engineered nanoparticle species. This will help to identify particle species/physicochemical properties that are noxious for healing wounds, but may also discover those that are beneficial for healing wounds.

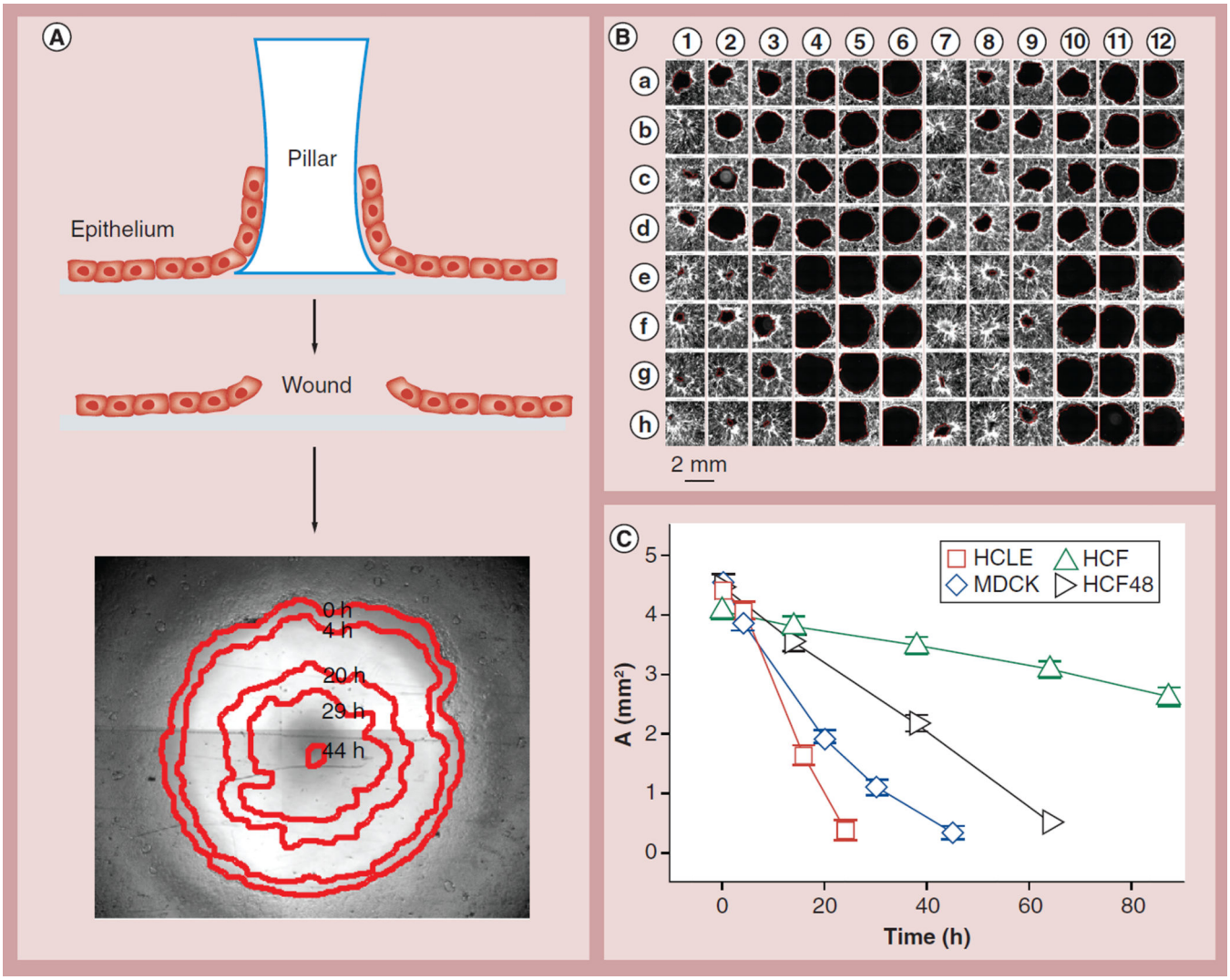

Figure 1. The circular wound array bioassay

(A) Cells were plated onto a substrate with a circular region blocked by a polydimethylsiloxane pillar (top). The pillar is peeled off to create a circular wound (middle). The 2-mm wound in an MDCK cell monolayer heals over 48 h (bottom); the leading edge at five time points (red edges) is tracked automatically by image analysis and overlaid onto the original wound. **(B)** In a single experiment, 96 wounds are followed and shown here after healing for approximately 24 h. In this example, HCLE cells, stained with 5-chloromethylfluorescein diacetate (Invitrogen, CA, USA), have been treated with 0–100 μg/ml CuO (rows a–d) and ZnO (rows e–h) ENPs, either aged for 1 week in aqueous suspension (columns 1–6) or freshly prepared (columns 7–12). **(C)** Different cells in the absence of any treatment healed wounds at different rates. The initial wound area is slightly larger than that of a 2-mm diameter circle due to the detachment of some cells abutting the stamp. Mean ±1.96 standard error of the mean; nonoverlapping error bars indicate statistically significant difference ($p < 0.05$); $n \geq 24$ wells from at least four experiments. HCF: Human corneal fibroblast; HCLE: Human corneal limbal epithelial; MDCK: Madin–Darby canine kidney.

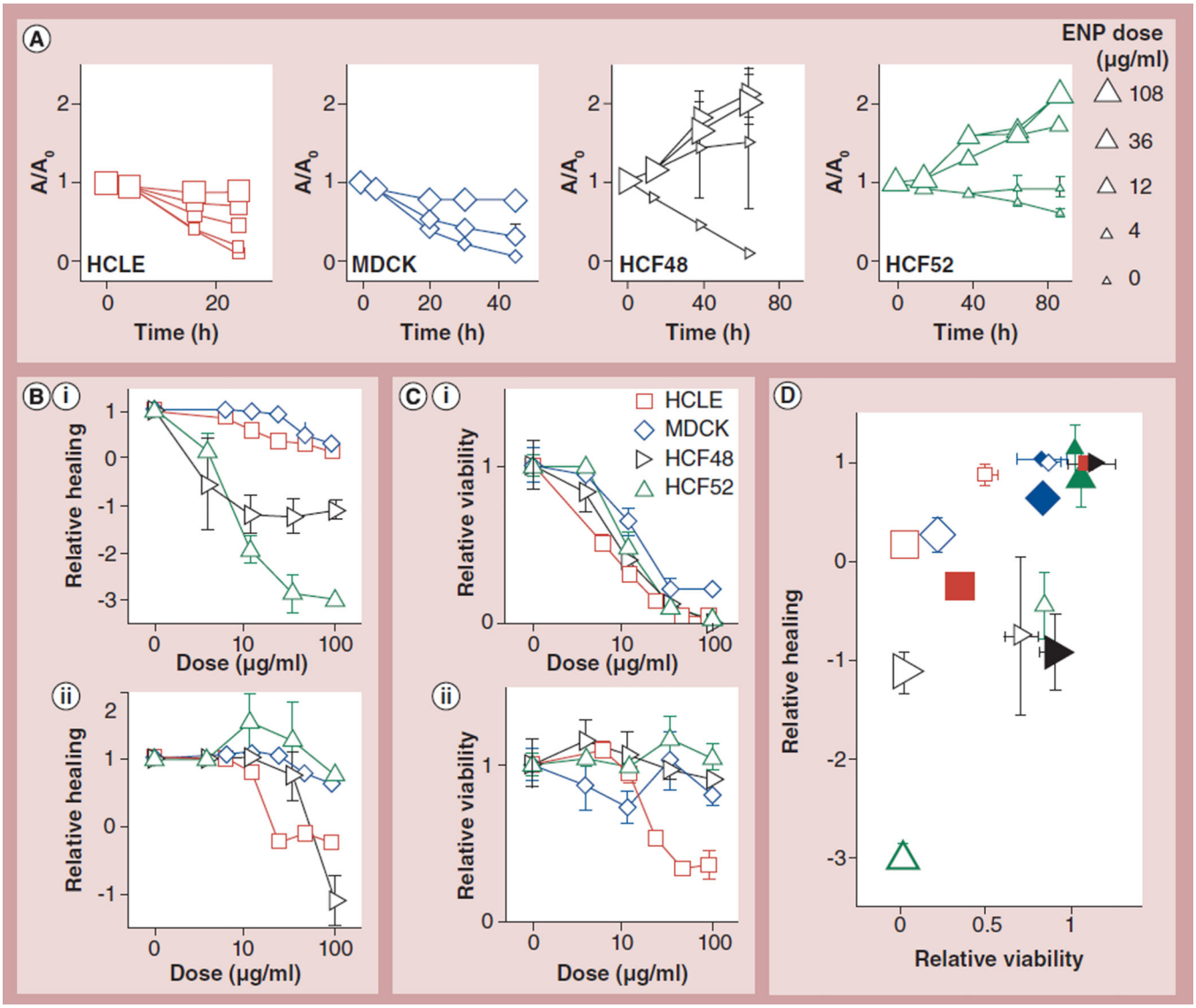

Figure 2. CuO and ZnO engineered nanoparticles impacted wound healing and viability in a cell type-dependent manner

(A) CuO ENPs slow down the wound healing process in a dose- and cell type-dependent manner. A/A_0 is the normalized wound area, where A and A_0 are the wound area at time t and 0 h, respectively. ENP doses are in μg/ml with large marker sizes representing higher doses. **(B)** The dose dependence of relative healing is depicted for four cell types treated with **(B,i)** CuO or **(B,ii)** ZnO. See text for the definition of relative healing. **(C)** The dose dependence of relative viability is depicted for cells treated with **(C,i)** CuO or **(C,ii)** ZnO. **(D)** The reduction in wound healing is associated with, but can greatly exceed, the reduction in cell viability. Data symbols mean the same for **(B–D)**, except for **(D)**, where the small and large symbols are for 6.25 and 100 μg/ml, respectively, and the open and filled symbols are for CuO and ZnO ENPs, respectively. Mean ±1.96 standard error of the mean; nonoverlapping error bars indicate statistically significant difference ($p < 0.05$); $n \geq 6$ wells from at least two independent experiments.

HCLE: Human corneal limbal epithelial cells; HCF: Human corneal fibroblasts; MDCK: Madin–Darby canine kidney.

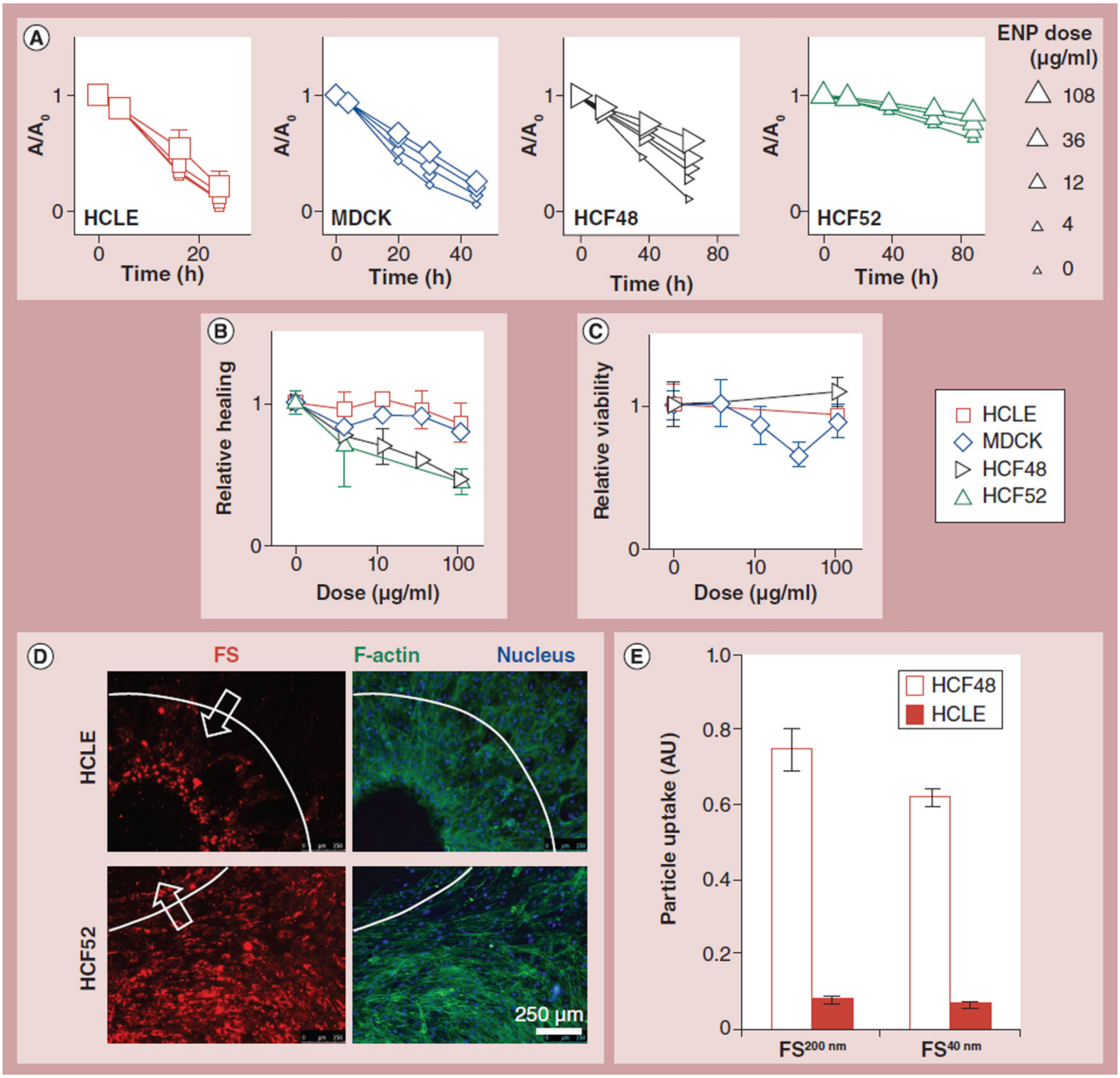

Figure 3. Engineered nanoparticles can impede wound healing without reducing cell viability

Carboxylated, polystyrene ENPs (40 nm; FS^{40nm}) **(C)** do not decrease cell viability but **(A & B)** slow down wound healing in a dose-and cell type-dependent manner. **(D)** The patterns of particle deposition are distinct between HCLE and HCF52 cells. White dash lines and arrows mark the original wound and the direction of healing, respectively. **(E)** Particle uptake is higher for HCF48 cells than for HCLE cells. Confluent cells were treated for 1 day with 12 μg/ml of FS of two sizes, and then subjected to fixation/permeabilization before fluorescent particles were quantified using a plate reader. Mean ±1.96 standard error of the mean; nonoverlapping error bars indicate statistically significant difference ($p < 0.05$); n = 6–12 wells from two experiments.

FS: FluoSpheres® (Invitrogen, CA, USA); HCLE: Human corneal limbal epithelial cells; HCF: Human corneal fibroblasts; MDCK: Madin–Darby canine kidney.

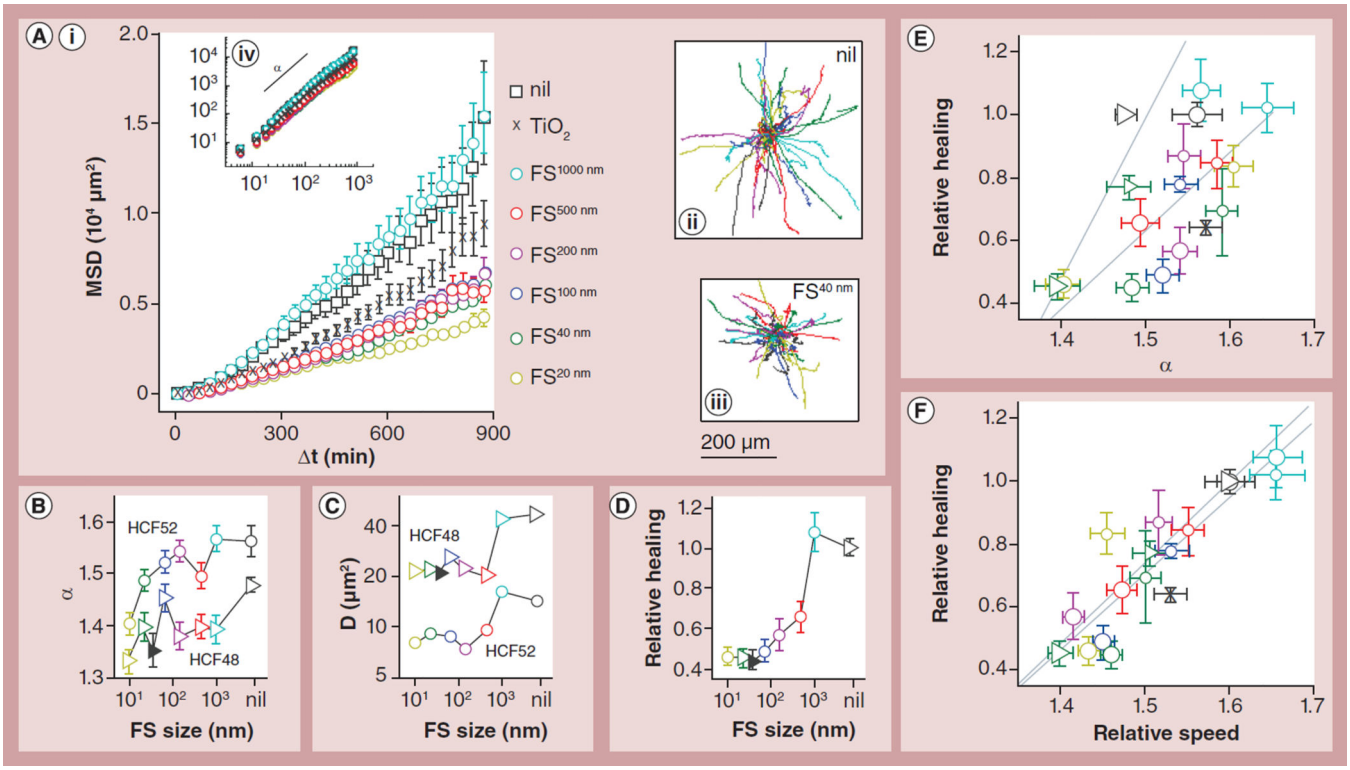

Figure 4. Reduction in single cell migration explains impeded wound healing

Impeded wound healing of HCF cells by FS particles was associated with impeded single cell migration in a particle size-dependent manner. **(A)** The trajectories of individual cells were obtained **(A,ii)** without treatment or with particle treatment (e.g., **[A,iii]** with FS^{40nm}). For every condition, the MSD increased as a power law function of the time lag, Δt (**[A,iv]** logarithmic scale), although the effect of nanoparticles becomes more apparent when plotted in linear scale. All particles were applied at 108 μg/ml except when noted otherwise. **(B & C)** We fitted the MSD data using $MSD = D\frac{\Delta t^{\alpha}}{10}$ to obtain directional persistence, α (panel B), and speed, *D* (panel C), for HCF52 cells (circles) and HCF48 cells (triangles). Both α and *D* are reduced by FS treatment in a particle size-dependent manner, with smaller particles exerting a larger effect. **(D)** Using the CWAB assay, we found relative healing is also retarded by FS in a similar size-dependent manner. The filled triangles in **(B–D)** are for nonfluorescent PS^{60nm} particles. **(E & F)** Relative healing exhibited positive correlation with both **(E)** α and **(F)** relative migration speed, defined as the cell speed normalized by that of untreated cells. Triangles represent HCF48, circles HCF52, and crosses HCF52 treated with TiO_2 ENPs; particle types are distinguished by color as indicated in **(A)**. The data points from each donor are fitted by the dotted lines. Mean ± standard error of the mean; for single cell migration, n = 135–679 cells from two independent experiments for HCF52 and one experiment for HCF48; for wound healing, n = 3–9 wells with particle treatments and n = 24–54 wells without treatments.

CWAB: Circular wound array bioassay; FS: FluoSpheres® (Invitrogen, CA, USA); HCLE: Human corneal limbal epithelial cells; HCF: Human corneal fibroblasts; MDCK: Madin-Darby canine kidney; MSD: Mean squared displacement; PS: Polystyrene.

Table 1

Properties of engineered nanoparticle suspensions in two cell culture media.

Material	DMEM/F12 with 10% FBS and 10 ng/ml EGF			Low-glucose DMEM with 10% FBS		
	d_H (nm)	PdI	ζ (mV)	d_H (nm)	PdI	ζ (mV)
SiO_2	172 ± 1.50	0.360 ± 0.003	−10.3 ± 0.666	367 ± 14.5	0.530 ± 0.106	−9.60 ± 0.475
CuO	203 ± 8.44	0.984 ± 0.028	−9.43 ± −0.497	288 ± 12.9	0.240 ± 0.021	−8.55 ± 0.447
ZnO	162 ± 9.54	0.564 ± 0.046	−9.31 ± 1.25	1210 ± 947	0.867 ± 0.148	−6.23 ± 2.53
TiO_2	838 ± 4.31	0.521 ± 0.055	−18.5 ± 9.67	868 ± 15.0	0.499 ± 0.097	−8.35 ± 4.39
$FS^{20\ nm}$	124 ± 15.6	0.421 ± 0.075	−12.3 ± 1.22	110 ± 2.65	0.359 ± 0.086	−9.89 ± 7.03
$FS^{40\ nm}$	92.3 ± 3.81	0.307 ± 0.008	−17.7 ± 5.0	95.6 ± 0.767	0.268 ± 0.006	−29.2 ± 4.44
$FS^{100\ nm}$	203 ± 0.802	0.300 ± 0.012	−22.4 ± 10.6	182 ± 2.25	0.199 ± 0.015	−6.15 ± 4.39
$FS^{200\ nm}$	279 ± 2.36	0.114 ± 0.013	−4.26 ± 7.46	319 ± 25.9	0.144 ± 0.048	−12.8 ± 4.80
$FS^{500\ nm}$	550 ± 3.96	0.255 ± 0.041	−12.7 ± 1.55	605 ± 3.78	0.214 ± 0.013	−7.61 ± 4.98
$FS^{1000\ nm}$	1050 ± 33.2	0.865 ± 0.013	−6.31 ± 3.04	927 ± 206	0.689 ± 0.039	−8.43 ± 7.26
$PS^{60\ nm}$ COOH	88.4 ± 1.93	0.313 ± 0.002	−29.2 ± 17.1	91.6 ± 1.91	0.262 ± 0.007	−13.1 ± 8.72
$PS^{60\ nm}$ naked	91.5 ± 1.94	0.306 ± 0.005	−6.36 ± 8.62	97.4 ± 2.25	0.269 ± 0.003	−14.4 ± 4.67

dH: Hydrodynamic diameter; F12: Nutrient Mixture F-12; FBS: Fetal bovine serum; FS: FluoSpheres® (Invitrogen, CA, USA); PdI: Polydispersity index; PS: Polystyrene; ζ: Zeta-potential.

Nanomedicine (Lond). Author manuscript; available in PMC 2015 December 18.